Advanced Journal of Science, Technology and Engineering
ISSN: 2997-5972
Volume 6, Issue 1, 2026 (pp. 60-87)
www.abjournals.org

NOVEL PREDICTIVE CURRENT CONTROL OF PERMANENT MAGNET SYNCHRONOUS MACHINE: DBC AND FOC ALGORITHMS

Ibrahim Massaquoi[1*] and Alfred Abu[2].

[1]Basic and Environmental Sciences, Eastern Technical University, Sierra Leone.
Email: ibrahim@etusl.edu.sl

[2]Physics, Njala University, Sierra Leone.
Email: aabu@njala.edu.sl

[*]Corresponding Author's Email: ibrahim@etusl.edu.sl

Cite this article:

Ibrahim Massaquoi, Alfred Abu (2026), Novel Predictive Current Control of Permanent Magnet Synchronous Machine: DBC and FOC Algorithms. Advanced Journal of Science, Technology and Engineering 6(1), 60-87. DOI: 10.52589/AJSTE-J8Z7SLJ8

Manuscript History

Received: 18 Mar 2026

Accepted: 20 Apr 2026

Published: 15 Jun 2026

ABSTRACT: *Introduction: This work presents a novel predictive current control methodology for Permanent Magnet Synchronous Motors (PMSM). The study develops a dq-model of the PMSM in the rotor reference frame and establishes discretized motor models to facilitate the implementation of advanced control algorithms. The primary focus was on designing and evaluating a Dead-Beat Predictive Control (DBC) algorithm and comparing its performance with the conventional Field-Oriented Control (FOC) algorithm, which was developed due to its technological maturity and similarities with predictive methods. Methods: A complete closed-loop control system for PMSM was constructed using MATLAB/Simulink, incorporating the DBC and FOC algorithms. The FOC relied on PI controllers, whose tuning was optimized through a first-principles tuning algorithm. Both control schemes aimed to ensure that the dq-currents accurately tracked their references, thus controlling speed, torque, and rotor position effectively. Additionally, Space Vector Pulse Width Modulation (SVPWM) was implemented with an optimized switching sequence to minimize losses and harmonic distortion. The inverter switching strategy involved dividing the switching period into segments, applying zero and active vectors symmetrically, and analyzing the rectifier operation across different angle regions. Results: Simulation results demonstrated that both the DBC and FOC models effectively tracked current and speed references with minimal transients. The DBC exhibited a faster response, settling within approximately 0.12 seconds, 40% quicker than the FOC, which settled in 0.2 seconds without overshoot. During speed reversals, the DBC maintained sinusoidal phase currents with minor drops, and the d-axis current remained effectively at zero with deviations near 10^(-17). The system achieved a rapid speed response, reaching 500 RPM within 0.2 seconds, with the phase currents remaining balanced and sinusoidal. The FOC showed about 16% overshoot but still provided a very fast response, making it suitable for applications where rapid response is critical. Conclusion: The developed DBC and FOC algorithms successfully controlled PMSM, with the DBC demonstrating superior speed response and quicker settling times. Both methods maintained stable, sinusoidal phase currents and precise current tracking during transient conditions such as speed reversals. The simulation results validate that the proposed predictive control approach (DBC) offers improved performance over the conventional FOC, making it a promising candidate for high-performance motor control applications requiring fast dynamic response and minimal transient disturbance.*

KEYWORDS*:* Algorithm, Predictive, Control, Current, Deadbeat, Magnet, Permanent, etc.

Article DOI: 10.52589/AJSTE-J8Z7SLJ8
DOI URL: https://doi.org/10.52589/AJSTE-J8Z7SLJ8

Advanced Journal of Science, Technology and Engineering
ISSN: 2997-5972
Volume 6, Issue 1, 2026 (pp. 60-87)
www.abjournals.org

INTRODUCTION

The Permanent Magnet Synchronous Motor (PMSM) surpasses induction motors of comparable size in several key aspects, including higher power density, improved efficiency, and a superior torque-to-inertia ratio. These advantages have spurred extensive research into its design, analysis, and control strategies. While fixed-speed operation may be adequate for low-precision tasks, many industrial applications require precise control of speed and torque, leading to the adoption of Adjustable Speed Drives (ASD) **[3,5]**.

Various control techniques, such as Field-Oriented Control (FOC) and Dead-Beat Predictive Control (DBC), facilitate PMSM speed regulation. Predictive control methods utilize system models to forecast future behaviour, with DBC standing out as a notable example **[2]**. DBC excels in managing complex systems with multiple inputs and outputs by predicting dq-axis currents, thereby enhancing reference tracking, minimizing ripples, and eliminating steady-state errors. Its primary focus was on rapidly aligning actual currents with their references, ensuring swift dynamic response.

While FOC was a well-established and widely adopted control approach that employs PI controllers within a dq reference frame, it can pose challenges related to the tuning process. Improper tuning may lead to control inaccuracies. Conversely, DBC, which predicts system states to determine control actions, offers notable advantages over traditional PI/PID-based methods, particularly in systems with multiple inputs and outputs **[16]**.

In PMSM drives, controlling the q-axis current linked to torque and speed was typically achieved through a current control strategy that processes the speed error via a PI controller. This study compares the performance of FOC and predictive algorithms like DBC for PMSM control within MATLAB/Simulink environments **[1]**.

Despite their benefits, all two methods, FOC and DBC, were susceptible to high current and torque ripples, especially in predictive control schemes. Such ripples were detrimental in high-precision applications, which motivates ongoing research into improving drive performance and refining PI tuning techniques for FOC.

This research aims to evaluate and compare the effectiveness of FOC and DBC in PMSM control, emphasizing the importance of advanced tuning methods and ripple reduction strategies to meet industrial standards. The core objective was to develop a novel predictive current control scheme for PMSMs. Specifically, the research objectives were:

1. To develop a dead-beat control (DBC) algorithm that ensures the reference current matches the predicted next current for rapid and accurate current tracking.

2. To design a self-tuned FOC system and compare its performance with the proposed DBC and other predictive control methods.

Article DOI: 10.52589/AJSTE-J8Z7SLJ8
DOI URL: https://doi.org/10.52589/AJSTE-J8Z7SLJ8

LITERATURE REVIEW

Dead-Beat Control (DBC) originally emerged within the chemical processing industry, characterized by complex, dynamic systems with numerous inputs and outputs. It functions by solving nonlinear control equations at each sampling interval, utilizing the current state of the plant to forecast and optimize future control actions while adhering to operational constraints. Early implementations included Model Predictive Heuristic Control (MPHC) and Dynamic Matrix Control (DMC), both of which relied on plant models to minimize control errors through future predictions **[6]**.

In recent years, DBC has broadened its application scope to fields such as manufacturing, aerospace, energy, healthcare, and environmental management, demonstrating its technological evolution beyond traditional industrial settings. Significant advancements include the development of predictive control strategies for electric motors, particularly Permanent Magnet Synchronous Motors (PMSMs), tackling issues like sampling delays, parameter variations, current ripples, and torque optimization. Researchers have introduced various robust, adaptive, and multi-vector control approaches to enhance accuracy, reduce ripple effects, and improve transient response **[7,8]**.

Major innovations encompass the integration of disturbance observers, the optimization of voltage vectors, and the adoption of advanced techniques such as fuzzy logic, space vector modulation, and sensorless control methods. Despite these progressions, several challenges remain, including the need for methods that directly predict stator voltages without relying on cost functions, simplifying control algorithms to lessen computational demands, and establishing analytical tuning methods for PI controllers within Field-Oriented Control (FOC) frameworks **[10]**.

METHODOLOGY

dq-Modelling of the Permanent Magnet Synchronous Machine (PMSM)

The dq-model of the PMSM was derived from a simplified two-phase representation aligned with the direct (d) and quadrature (q) axes, chosen for its simplicity. Since the rotor consists solely of magnets with no windings, magnetic flux linkages are modelled as a flux source concentrated along one axis **[8]**.

The physical model of the machine was depicted in *Figure 1*, and the corresponding circuit model in the stator reference frame is derived accordingly. However, because inductances vary with rotor position, this model isn't ideal for analysis. To address this, a transformation to a rotor-synchronous reference frame is performed, rendering the inductances constant. The derivation relies on these assumptions: ***(1)*** Stator windings are balanced with sinusoidally distributed magnetomotive force (mmf). ***(2)*** Inductance varies sinusoidally with rotor position. ***(3)*** Effects of saturation and parameter variations are neglected, and ***(4)*** the machine does not include damping circuits.

Figure 1 illustrates a two-phase, two-pole PMSM, with the q-axis displaced 90 electrical degrees from the d-axis. The flux linkage was concentrated at an angle θ_r from the d-axis, with current directions and voltage polarities shown accordingly **[9]**.

ISSN: 2997-5972
Volume 6, Issue 1, 2026 (pp. 60-87)

Figure 1: Physical model of a two-phase, two-pole PMSM

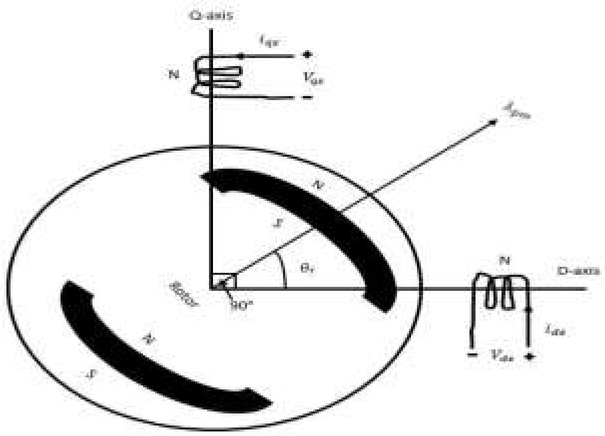

The stator d-axis and q-axis voltages are the sum of the resistive drop derivative of their respective flux linkages, as given in equations 1 and 2. Since the windings were balanced, the resistances were equal, i.e. $R_q = R_d = R_s$.

$$V_{qs} = R_s i_{qs} + \frac{d}{dt}\lambda_{qs} \tag{1}$$

$$V_{ds} = R_s i_{ds} + \frac{d}{dt}\lambda_{ds} \tag{2}$$

The stator flux linkage is the sum of self-flux linkages and mutual flux linkages.

$$\lambda_{qs} = L_{qq}i_{qs} + L_{qd}i_{ds} + \lambda_{pm}sin\theta_r \tag{3}$$

$$\lambda_{ds} = L_{dd}i_{ds} + L_{qd}i_{qs} + \lambda_{pm}cos\theta_r \tag{4}$$

Substituting 3 and 4 into 1 and 2, respectively;

$$V_{qs} = R_s i_{qs} + i_{qs}\frac{d}{dt}L_{qq} + L_{qq}\frac{d}{dt}i_{qs} + L_{qd}\frac{d}{dt}i_{ds} + i_{ds}\frac{d}{dt}L_{qd} + \lambda_{pm}\frac{d}{dt}(sin\theta_r) \tag{5}$$

$$V_{ds} = R_s i_{ds} + i_{ds}\frac{d}{dt}L_{dd} + L_{dd}\frac{d}{dt}i_{ds} + L_{qd}\frac{d}{dt}i_{qs} + i_{qs}\frac{d}{dt}L_{qd} + \lambda_{pm}\frac{d}{dt}(cos\theta_r) \tag{6}$$

Where L_{qq} and L_{dd} are respectively the self-inductances of the q-axis and d-axis windings, Lqd was the mutual inductance between the q and d axes measured along the q-axis, and L_{dq} was the mutual inductance between the d and q axes measured along the d-axis.

Inductances as Functions of Rotor Position

Looking at Figure 1 above and considering the inductance of d-axis when the rotor position θ_r = 0, the magnetic axis was aligned with d-axis and d-axis flux was maximum, thus resulting in maximum d-axis inductance L_d. Also, when rotor position $\theta_r = 90°$, the magnetic axis is aligned with the q-axis, and the d-axis flux is minimum, thus resulting in minimum d-axis inductance L_q. Since mmf was assumed to be sinusoidal, the self-inductances of both d and q axes can be modelled as cosine functions of rotor position from the d-axis, as in 7 and 8

Article DOI: 10.52589/AJSTE-J8Z7SLJ8
DOI URL: https://doi.org/10.52589/AJSTE-J8Z7SLJ8

$$L_{qq} = \frac{1}{2}[(L_q + L_d) + (L_q - L_d)\cos(2\theta_r)] \quad 7$$

$$L_{dd} = \frac{1}{2}[(L_q + L_d) - (L_q - L_d)\cos(2\theta_r)] \quad 8$$

It can be verified from 8 that at $\theta_r = 0°$, $L_{dd} = L_d$ and at $\theta_r = 90°$, $L_{dd} = L_q$.

We can simplify 7 and 8 by substituting $\frac{1}{2}(L_q + L_d) = L_1$ and $\frac{1}{2}(L_q - L_d) = L_2$

so that we obtain;

$L_{qq} = L_1 + L_2 cos\ (2\theta_r)$ 9

$L_{dd} = L_1 - L_2 cos\ (2\theta_r)$ 10

In a surface-mounted or one with a cylindrical rotor, there was no saliency, and the mutual inductance between the d and q axes was zero **[11]**. In an interior PMSM, there was saliency, which causes uneven reluctance. The mutual inductance in this case was maximum when the rotor position is 45° and zero when the rotor position is 0° or 90°. Assuming sinusoidal mmf, the mutual inductance becomes;

$$L_{qd} = \frac{1}{2}(L_d - L_q)sin(2\theta_r) = -L_2\sin(2\theta_r) \quad 11$$

Substituting 9, 10 and 11 into 5 and 6 and noting that:

$$\frac{d}{dt}(sin\theta_r) = \frac{d(sin\theta_r)}{d\theta_r}\frac{d\theta_r}{dt} = \omega_r cos\theta_r$$
$$\frac{d}{dt}(cos\theta_r) = \frac{d(cos\theta_r)}{d\theta_r}\frac{d\theta_r}{dt} = -\omega_r sin\theta_r$$
$$\frac{d}{dt}(L_{qq}) = \frac{d}{dt}(L_1 + L_2cos(2\theta_r)) = -2\omega_r L_2\sin(2\theta_r)$$
$$\frac{d}{dt}(L_{dd}) = \frac{d}{dt}(L_1 - L_2cos(2\theta_r)) = 2\omega_r L_2\sin(2\theta_r)$$
$$\frac{d}{dt}(L_{qd}) = \frac{d}{dt}(-L_2\sin(2\theta_r)) = -2\omega_r L_2\cos(2\theta_r)$$

We obtain 12

$$\begin{bmatrix} V_{qs} \\ V_{ds} \end{bmatrix} = R_s \begin{bmatrix} i_{qs} \\ i_{ds} \end{bmatrix} + \begin{bmatrix} L_1 + L_2\cos(2\theta_r) & -L_2\sin(2\theta_r) \\ -L_2\sin(2\theta_r) & L_1 - L_2\cos(2\theta_r) \end{bmatrix} \frac{d}{dt} \begin{bmatrix} i_{qs} \\ i_{ds} \end{bmatrix} +$$
$$2\omega_r L_2 \begin{bmatrix} -sin2\theta_r & -cos2\theta_r \\ -cos2\theta_r & \sin2\theta_r \end{bmatrix} \begin{bmatrix} i_{qs} \\ i_{ds} \end{bmatrix} + \lambda_{pm}\omega_r \begin{bmatrix} cos\theta_r \\ -sin\theta_r \end{bmatrix} \quad 12$$

In surface-mounted PMSM, $L_q = L_d$ and $L_2 = 0$. Equation 12 reduces to

Article DOI: 10.52589/AJSTE-J8Z7SLJ8
DOI URL: https://doi.org/10.52589/AJSTE-J8Z7SLJ8

$$\begin{bmatrix} V_{qs} \\ V_{ds} \end{bmatrix} = R_s \begin{bmatrix} i_{qs} \\ i_{ds} \end{bmatrix} + \begin{bmatrix} L_1 & 0 \\ 0 & L_1 \end{bmatrix} \frac{d}{dt} \begin{bmatrix} i_{qs} \\ i_{ds} \end{bmatrix} + \lambda_{pm}\omega_r \begin{bmatrix} cos\theta_r \\ -sin\theta_r \end{bmatrix} \quad 13$$

In the stator reference frame, the inductances of a salient pole machine were dependent on rotor position, making the voltage equation cumbersome. For steady state and dynamic studies, it was more convenient that the inductances be independent of rotor position. This was the essence of the transformation to the rotor reference frame.

Reference Frame Transformation

Let us assume that there exists a reference frame rotating at the same speed as the rotor and that the q^r and d^r-axes windings on the fictitious stator associated with this reference frame produce similar mmf as the actual stator on the q and d-axes. Let the q^r and d^r-axes of this fictitious stator be displaced from the q and d axes of the actual stator, respectively, by θ_r as shown in Figure 2, and resolving the vectors and summing up gives 14 and 15 **[18].**

Figure 2: Stationery and Rotor Reference Frame

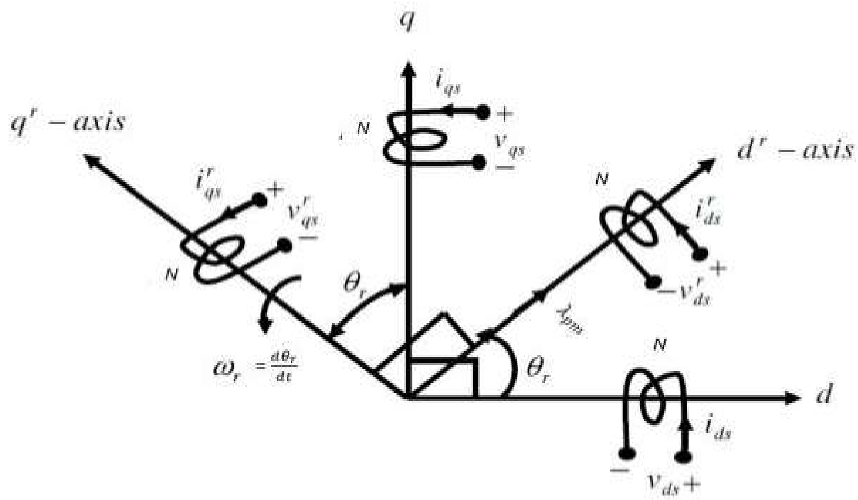

$$Ni_{qs} = Ni^r_{qs}cos\theta_r + Ni^r_{ds}sin\theta_r \quad 14$$

$$Ni_{ds} = -Ni^r_{qs}sin\theta_r + Ni^r_{ds}cos\theta_r \quad 15$$

In matrix form;

$$\begin{bmatrix} i_{qs} \\ i_{ds} \end{bmatrix} = \begin{bmatrix} cos\theta_r & sin\theta_r \\ -sin\theta_r & cos\theta_r \end{bmatrix} \begin{bmatrix} i^r_{qs} \\ i^r_{ds} \end{bmatrix} \quad 16$$

The matrix $\begin{bmatrix} cos\theta_r & sin\theta_r \\ -sin\theta_r & cos\theta_r \end{bmatrix}$ transforms the currents from the stator to the rotor reference frame. The reverse transformation can also be performed using the inverse of the matrix, so that

Article DOI: 10.52589/AJSTE-J8Z7SLJ8
DOI URL: https://doi.org/10.52589/AJSTE-J8Z7SLJ8

$$\begin{bmatrix} i_{qs}^r \\ i_{ds}^r \end{bmatrix} = \begin{bmatrix} cos\theta_r & sin\theta_r \\ -sin\theta_r & cos\theta_r \end{bmatrix}^{-1} \begin{bmatrix} i_{qs} \\ i_{ds} \end{bmatrix} = \begin{bmatrix} cos\theta_r & -sin\theta_r \\ sin\theta_r & cos\theta_r \end{bmatrix} \begin{bmatrix} i_{qs} \\ i_{ds} \end{bmatrix} \quad 17$$

Similarly, the stator voltages can be transformed

$$\begin{bmatrix} V_{qs} \\ V_{ds} \end{bmatrix} = \begin{bmatrix} cos\theta_r & sin\theta_r \\ -sin\theta_r & cos\theta_r \end{bmatrix} \begin{bmatrix} V_{qs}^r \\ V_{ds}^r \end{bmatrix} \quad 18$$

The inverse transformation becomes

$$\begin{bmatrix} V_{qs}^r \\ V_{ds}^r \end{bmatrix} = \begin{bmatrix} cos\theta_r & sin\theta_r \\ -sin\theta_r & cos\theta_r \end{bmatrix}^{-1} \begin{bmatrix} V_{qs} \\ V_{ds} \end{bmatrix} = \begin{bmatrix} cos\theta_r & -sin\theta_r \\ sin\theta_r & cos\theta_r \end{bmatrix} \begin{bmatrix} V_{qs} \\ V_{ds} \end{bmatrix} \quad 19$$

Substituting 16 and 18 into 12 and simplifying, we get the PMSM model in rotor reference frame, which was equation 20 below

$$\begin{bmatrix} V_{qs}^r \\ V_{ds}^r \end{bmatrix} = \begin{bmatrix} R_s + L_q \frac{d}{dt} & \omega_r L_d \\ -\omega_r L_q & R_s + L_d \frac{d}{dt} \end{bmatrix} \begin{bmatrix} i_{qs}^r \\ i_{ds}^r \end{bmatrix} + \begin{bmatrix} \omega_r \lambda_{pm} \\ 0 \end{bmatrix} \quad 20$$

We see from equation 20 that in the rotor reference frame, the inductances are independent of rotor position.

Derivation of PMSM Power and Torque Equations

The total input power to the machine in the abc-reference frame is expressed as

$$P_{in} = V_a i_a + V_b i_b + V_c i_c \quad 21$$

A transformation from abc – qdo (rotor reference frame), known as Park's transform, was defined as follows

$$i_{qd0}^r = [T_{abc}] i_{abc} \quad 22$$

$$i_{abc} = [T_{abc}]^{-1} i_{qd0}^r \quad 23$$

where

$$T_{abc} = \frac{2}{3} \begin{bmatrix} cos\theta_r & \cos\left(\theta_r - \frac{2\pi}{3}\right) & \cos\left(\theta_r + \frac{2\pi}{3}\right) \\ sin\theta_r & \sin\left(\theta_r - \frac{2\pi}{3}\right) & \sin\left(\theta_r + \frac{2\pi}{3}\right) \\ \frac{1}{2} & \frac{1}{2} & \frac{1}{2} \end{bmatrix} \quad 24$$

Similarly

$$V_{abc} = [T_{abc}]^{-1} V_{qd0}^r \quad 25$$

Article DOI: 10.52589/AJSTE-J8Z7SLJ8
DOI URL: https://doi.org/10.52589/AJSTE-J8Z7SLJ8

Advanced Journal of Science, Technology and Engineering
ISSN: 2997-5972
Volume 6, Issue 1, 2026 (pp. 60-87)

Substituting 23 and 25 into 21 gives

$$P_{in} = \frac{3}{2}\left[\left(V_{qs}^{r} i_{qs}^{r} + V_{ds}^{r} i_{ds}^{r}\right) - 2V_0 i_0\right] \qquad 26$$

If we assume that the system was balanced, then

$i_0 = i_a + i_b + i_c = 0$

Equation 26 then reduces to

$$P_{in} = \frac{3}{2}\left(V_{qs}^{r} i_{qs}^{r} + V_{ds}^{r} i_{ds}^{r}\right) \qquad 27$$

Substituting 26 into 27 and rearranging gives

$$P_{in} = \frac{3}{2}\left[\left(i_{qs}^{r2} R_s + i_{ds}^{r2} R_s\right) + \left(L_q \frac{d}{dt} i_{qs}^{r2} + L_d \frac{d}{dt} i_{ds}^{r2}\right) + \left(\omega_r L_d i_{ds}^{r} i_{qs}^{r} + \omega_r \lambda_{pm} i_{qs}^{r} - \omega_r L_q i_{qs}^{r} i_{ds}^{r}\right)\right] \qquad 28$$

We see from equation 28 that the power has three components, viz. The first component represents stator and rotor resistive losses. The second component represents the rate of change of stored magnetic energy. This component is zero at the steady state. The third component represents the mechanical power

So, the mechanical power P_m was given by

$$P_m = \omega_r L_d i_{ds}^{r} i_{qs}^{r} + \omega_r \lambda_{pm} i_{qs}^{r} - \omega_r L_q i_{qs}^{r} i_{ds}^{r} \qquad 29$$

The air gap was associated with rotor speed. It was the product of the air gap electromagnetic torque and the mechanical rotor speed that was

$$P_m = \omega_m T_e \; where \; \omega_r = \frac{P}{2}\omega_m \qquad 30$$

Substituting 30 into 29 gives

$$T_e = \frac{P_m}{\omega_m} = \frac{3}{2}\frac{P}{2}\left(\lambda_{pm} i_{qs}^{r} + \left(L_d - L_q\right) i_{qs}^{r} i_{ds}^{r}\right. \qquad 31$$

Permanent Magnet Synchronous Machine State Space Model

To further simplify the PMSM model, the superscript “r” for “rotor reference frame” and the subscript “s” for stator parameters are dropped, bearing in mind that stator parameters in the rotor reference frame are always implied. The simplified state space model of a PMSM in rotor reference frame was given by 32 – 35.

$$\frac{di_d}{dt} = \frac{1}{L_d} V_d - \frac{R}{L_d} i_d + \frac{L_q}{L_d} \omega_r i_q \qquad 32$$

$$\frac{di_q}{dt} = \frac{1}{L_q} V_q - \frac{R}{L_q} i_q - \frac{L_d}{L_q} \omega_r i_d - \frac{\lambda_{pm}\omega_r}{L_q} \qquad 33$$

Article DOI: 10.52589/AJSTE-J8Z7SLJ8
DOI URL: https://doi.org/10.52589/AJSTE-J8Z7SLJ8

$$T_e = 1.5p(\lambda_{pm} i_q + (L_d - L_q) i_d i_q \quad 34$$

$$\frac{d\omega_r}{dt} = \frac{1}{j}(T_e - B\omega_r - T_L) \ \ and \ \ \frac{d\theta_r}{dt} = \omega_r \quad 35$$

Making V_d and V_q subjects of equations 32 and 33 gives equations 36 and 37, respectively.

$$V_d = Ri_d + L_d \frac{di_d}{dt} - \omega_r L_q i_q \quad 36$$

$$V_q = Ri_q + L_q \frac{di_q}{dt} - \omega_r (L_d i_d + \lambda_{pm}) \quad 37$$

Rearranging equations 36 and 37, we obtain equations 38 and 39, respectively.

$$\frac{di_d(t)}{dt} = \frac{1}{L_d} V_d(t) - \frac{R}{L_d} i_d(t) + \omega(t) \frac{L_q}{L_d} i_q(t) \quad 38$$

$$\frac{di_q(t)}{dt} = \frac{1}{L_q} V_q(t) - \frac{R}{L_q} i_q(t) - \omega(t) \frac{L_d}{L_q} i_d(t) - \frac{\omega(t)\lambda_{pm}}{L_q} \quad 39$$

Discretization of PMSM Model

We adopt Newton's difference formula, which defines the derivative of a function f(t) with respect to time as given in equation 40

$$\frac{df(t)}{dt} = \lim_{\Delta t \to 0} \frac{f(t+\Delta t) - f(t)}{\Delta t} \quad 40$$

If we substitute f(t) = $i_d(t) and\ i_q(t)$ in turns, we obtain equations 41 and 42, respectively.

$$\frac{di_d(t)}{dt} = \lim_{\Delta t \to 0} \frac{i_d(t+\Delta t) - i_d(t)}{\Delta t} \quad 41$$

$$\frac{di_q(t)}{dt} = \lim_{\Delta t \to 0} \frac{i_q(t+\Delta t) - i_q(t)}{\Delta t} \quad 42$$

Substituting equation 41 into equation 38 and 42 into 39, we obtain equations 43 and 44, respectively;

$$\frac{i_d(t+\Delta t) - i_d(t)}{\Delta t} = \frac{1}{L_d} V_d(t) - \frac{R}{L_d} i_d(t) + \omega(t) \frac{L_q}{L_d} i_q(t) \quad 43$$

$$\frac{i_q(t+\Delta t) - i_q(t)}{\Delta t} = \frac{1}{L_q} V_q(t) - \frac{R}{L_q} i_q(t) - \omega(t) \frac{L_d}{L_q} i_d(t) - \frac{\omega(t)\lambda_{pm}}{L_q} \quad 44$$

If we set Δt equal to a fixed sampling time, T_s, then equations 43 and 44 become 45 and 46, respectively

$$\frac{i_d(t+T_s) - i_d(t)}{T_s} = \frac{1}{L_d} V_d(t) - \frac{R}{L_d} i_d(t) + \omega(t) \frac{L_q}{L_d} i_q(t) \quad 45$$

Article DOI: 10.52589/AJSTE-J8Z7SLJ8
DOI URL: https://doi.org/10.52589/AJSTE-J8Z7SLJ8

$$\frac{i_q(t+T_s)-i_q(t)}{T_s} = \frac{1}{L_q}V_q(t) - \frac{R}{L_q}i_q(t) - \omega(t)\frac{L_d}{L_q}i_d(t) - \frac{\omega(t)\lambda_{pm}}{L_q} \quad 46$$

If we let k represent the first sampling time, then k+1 represents the next sampling time. So that $f(t) \equiv f(k) and\ f(t+\Delta t) = f(t+T_s) \equiv f(k+1)$. Then equations 45 and 46 become 47 and 48, respectively

$$\frac{i_d(k+1)-i_d(k)}{T_s} = \frac{1}{L_d}V_d(k) - \frac{R}{L_d}i_d(k) + \omega(k)\frac{L_q}{L_d}i_q(k) \quad 47$$

$$\frac{i_q(k+1)-i_q(k)}{T_s} = \frac{1}{L_q}V_q(k) - \frac{R}{L_q}i_q(k) - \omega(t)\frac{L_d}{L_q}i_d(k) - \frac{\omega(k)\lambda_{pm}}{L_q} \quad 48$$

In order to isolate the variables for the next sample time, we multiply through equations 47 and 48 by T_s and collect terms. After collecting terms and simplifying, we obtain equations 49 and 50

$$i_d(k+1) = \frac{T_s}{L_d}V_d(k) + \left(1 - \frac{RT_s}{L_d}\right)i_d(k) + \frac{\omega(k)L_qT_s}{L_d}i_q(k) \quad 49$$

$$i_q(k+1) = \frac{T_s}{L_q}V_q(k) + \left(1 - \frac{RT_s}{L_q}\right)i_q(k) - \frac{\omega(k)L_dT_s}{L_q}i_d(k) - \frac{\omega(k)\lambda_{pm}T_s}{L_q} \quad 50$$

We can put equations 49 and 50 in matrix form as shown in 51

$$\begin{bmatrix} i_d(k+1) \\ i_q(k+1) \end{bmatrix} = \begin{bmatrix} 1 - \frac{RT_s}{L_d} & \frac{\omega(k)L_qT_s}{L_d} \\ -\frac{\omega(k)L_dT_s}{L_q} & 1 - \frac{RT_s}{L_q} \end{bmatrix} \begin{bmatrix} i_d(k) \\ i_q(k) \end{bmatrix} + \begin{bmatrix} \frac{T_s}{L_d} & 0 \\ 0 & \frac{T_s}{L_q} \end{bmatrix} \begin{bmatrix} V_d(k) \\ V_q(k) \end{bmatrix} + \begin{bmatrix} 0 \\ -\frac{\omega(k)\lambda_{pm}T_s}{L_q} \end{bmatrix} \quad 51$$

Field Orientation Control (FOC)

Field-Oriented Control was a well-established control algorithm for AC machines. It was implemented in this thesis to provide a fair comparison for the proposed predictive control algorithm **[5]**. Field-oriented control makes use of PI controllers to reduce the error in the controlled variable. Tuning of PI controllers was very problematic and usually prone to error. To mitigate this challenge, we have developed an analytical means of calculating the gains of the PI controllers **[3]**. The analysis was also presented in this section. The voltage source inverter (VSI) that was used in the rest of the work was controlled by space vector modulation; hence, the principle of space vector modulation was also presented in this work. Figure 3 was the block model of the Field Oriented Control (FOC) of PMSM using a voltage source inverter with space vector modulation.

Article DOI: 10.52589/AJSTE-J8Z7SLJ8
DOI URL: https://doi.org/10.52589/AJSTE-J8Z7SLJ8

Figure 3: Block Diagram of the proposed Field-Oriented Control

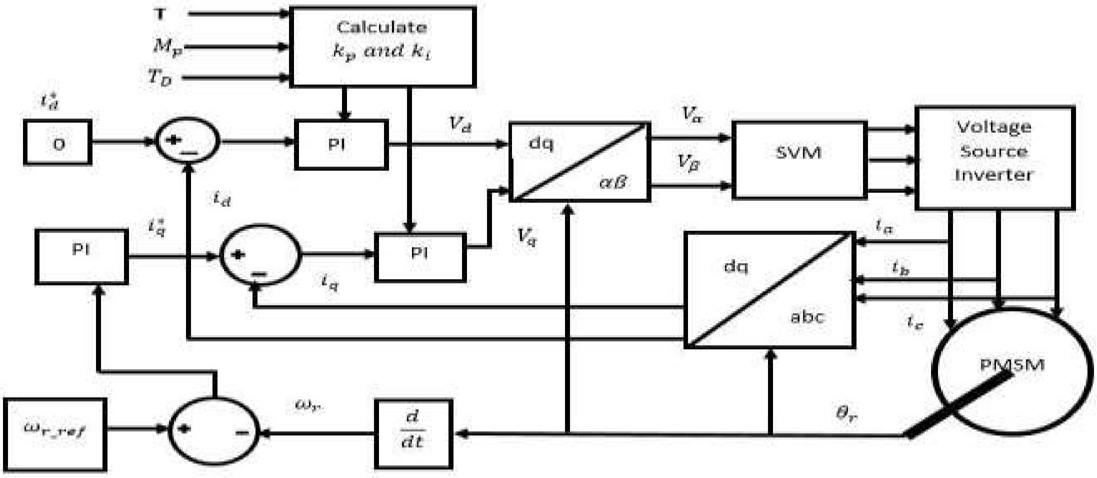

In FOC, the reference d-axis current was always maintained at zero in order to ensure the flux remains constant. The reference q-axis current was generated by comparing the reference speed with the actual motor speed and passing the speed error through a PI controller. The dq-axes current errors pass through PI controllers to produce dq-axes voltages (V_d, V_q), which, after dq-$\alpha\beta$ (Clarke's transform), becomethe reference voltage of the Space Vector Modulation block. It was seen from the motor model equation 3 that when $L_d = L_q$ (for a non-salient pole motor), the electromagnetic torque varies directly with q-axis current. Since speed was also proportional to torque, it then implies that current can control both speed and torque.

PI Controller Design

The expression for dq-axis voltages for a PMSM was given by 52 and 53

$$V_d = Ri_d + L_d\frac{di_d}{dt} - \omega L_q i_q \qquad 52$$

$$V_q = Ri_q + L_q\frac{di_q}{dt} + \omega(L_d i_d + \lambda_{pm}) \qquad 53$$

By transforming 52 and 53 to the frequency domain by the Laplace method, we get:

$$V_d(s) = (sL_d + R)i_d(s) - \omega L_q i_q(s) \qquad 54$$

$$V_q(s) = (sL_q + R)i_q(s) + \omega(L_d i_d(s) + \lambda_{pm}) \qquad 55$$

Since we were working with field-oriented current control (FOC) principle, we made the variable begin controlled (i.e. i_q subject of equation 55; i_q $current$ begin maintained at zero to ensure the flux remains constant. So, from 55 we get;

$$i_q(s) = [V_q(s) - \omega(L_d i_d(s) + \lambda_{pm}]\left(\frac{1}{sL_q + R}\right) \qquad 56$$

In block model form, equation 56 can be represented in Figure 4 below.

Article DOI: 10.52589/AJSTE-J8Z7SLJ8
DOI URL: https://doi.org/10.52589/AJSTE-J8Z7SLJ8

Advanced Journal of Science, Technology and Engineering
ISSN: 2997-5972
Volume 6, Issue 1, 2026 (pp. 60-87)

Figure 4: Block diagram of the open-loop current control model

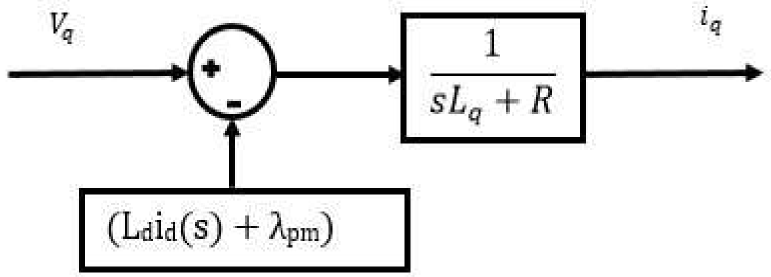

Equations 54 and 55 show that the presence of the back-emf expressions in the two equations makes the dq current control loops dependent. Thus, to achieve an independent current loop, the back-emf decoupling term was introduced. This decoupling term was included after the PI controller in the form of a disturbance with a similar value but opposite sign to the back-emf term in the motor equation. The block model of the system then becomes:

Figure 5: Block diagram of the closed-loop decoupled current control model

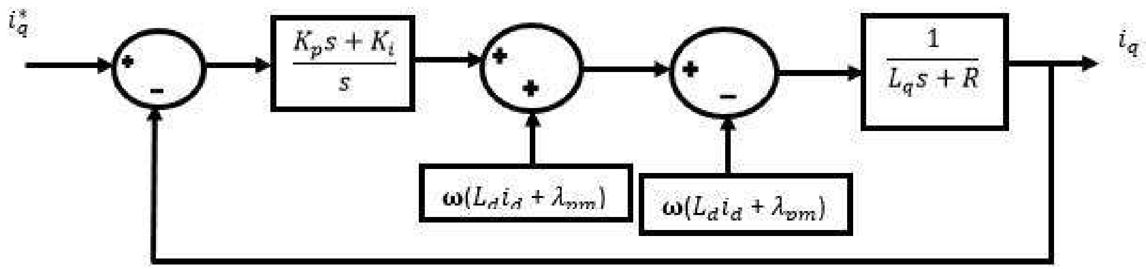

Since the effect of the back emf term was cancelled by the decoupling term, the system above reduces to Figure 6;

Figure 6: Block diagram of the closed-loop current control model

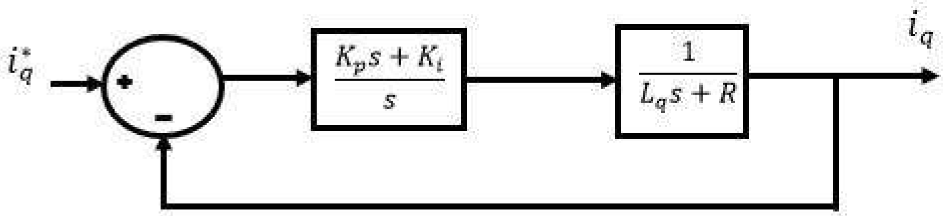

There was a computation time delay as well as a sensor response time delay inherent in the system; therefore, we introduce a first-order time delay as shown in Figure 7 below.

Article DOI: 10.52589/AJSTE-J8Z7SLJ8
DOI URL: https://doi.org/10.52589/AJSTE-J8Z7SLJ8

Advanced Journal of Science, Technology and Engineering
ISSN: 2997-5972
Volume 6, Issue 1, 2026 (pp. 60-87)
www.abjournals.org

Figure 7: Model for current control with time delay

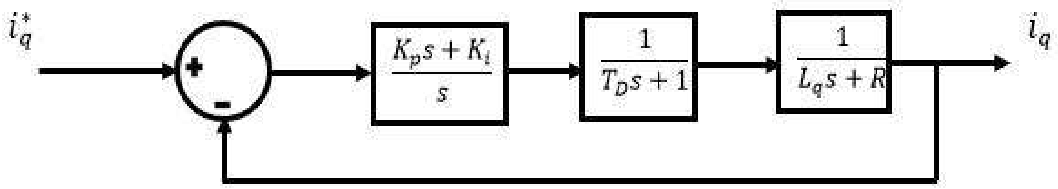

The transfer function of the open-loop system, G_{OL}, was given by 57.

$$G_{OL}(s) = \frac{K_p s + K_i}{s} \cdot \frac{1}{T_D s + 1} \cdot \frac{1}{Ls + R} \quad 57$$

If the zero of the PI controllers ($^{-}K_i/K_p$) was made to cancel out the pole ($^{-}R/L_d$) of the PMSM by a method known as pole-zero cancellation, then we set:

$$K_{ip} = \frac{K_i}{K_p} = \frac{R}{L} \quad \text{or } K_i. = K_p K_{ip}. \quad 58a$$

It was seen from 58a that the PI controller gains depend on machine parameters (R and L). During motor operation, the temperature was likely to increase due to losses occurring in the motor. When the temperature increases, resistance increases as well. To take care of the possible parameter variation due to temperature rise, we estimate the temperature of the winding with a Luenberger-type temperature observer given by 58b. It was reported that the difference between the reference flux and actual flux in the d-axis, $\Delta\lambda_d$, was proportional to the temperature rise. With the value of temperature, T, we can evaluate the resistance at any point in time, R(t), using equation 58c.

$$T = \frac{\Delta\lambda_d}{\lambda_{pm,ref} k_{Br}} \quad 58b$$

Where T was the temperature rise in °C, $\lambda_{pm,ref}$ was the permanent magnet flux measured at the reference temperature, k_{Br} was a constant whose value lies between $-0.0005/°C$ *and* $-0.001/°C$. The d-axis reference and actual flux were obtained by substituting the reference and actual d-axis current, respectively, in 2.

$$R(t) = R_0(1 + \alpha T) \quad 58c$$

Where R_0 is the room temperature resistance, T is the temperature rise, and α is the temperature coefficient of resistance ($\alpha = 0.0040$ /°C for copper). Substituting equation 58 into equation 57 gives equation 59.

$$G_{OL}(s) = \frac{K_p s + K_p K_{ip}}{s} \cdot \frac{1}{T_D s + 1} \cdot \frac{1}{Ls + R} \quad 59$$

Substituting $K_{ip} = \frac{R}{L}$ into equation 59 and simplifying gives:

Article DOI: 10.52589/AJSTE-J8Z7SLJ8
DOI URL: https://doi.org/10.52589/AJSTE-J8Z7SLJ8

$$G_{OL}(s) = \frac{K_p}{T_D L} \cdot \frac{1}{s(s+\frac{1}{T_D})} \quad 60$$

If we assume K=$\frac{K_p}{T_D L}$, then 60 becomes:

$$G_{OL}(s) = \frac{K}{s(s+\frac{1}{T_D})} \quad 61$$

For the closed loop system, the transfer function, G_{CL}, is given by:

$$G_{CL}(s) = \frac{G_{OL}(s)}{1+G_{OL}(s)} \quad 62$$

After making the substitution and simplifying, 62 changes to 63:

$$G_{CL}(s) = \frac{K}{s\left(s+\frac{1}{T_D}\right)+K} = \frac{K}{s^2+\frac{1}{T_D}s+K} \quad 63$$

The general second-order system transfer function was represented as 64:

$$H(s) = \frac{\omega_n^2}{s^2+2\xi\omega_n s+\omega_n^2} \quad 64$$

By comparing equations 63 and 64, we obtain equation 65

$$\omega_n=\sqrt{K} \text{ and } 2\xi\omega_n = \frac{1}{T_D} \text{ or } \xi = \frac{1}{2T_D\sqrt{K}} \quad 65$$

Where represents the natural frequency and the damping ratio. The maximum percentage overshoot for a second-order system is expressed as:

$$M_p = e^{-\pi\xi/\sqrt{1-\xi^2}} \quad 66$$

So, by choosing the value of T_D as well as the maximum percentage overshoot allowed, K_p and K_i can be computed using equations 65 and 66.

PI Controller Model

From equations 52 and 53, the time rate of change of dq-axes currents was given by equations 67 and 68, respectively.

$$\frac{di_d}{dt} = \frac{1}{L_d} i_d - \frac{R}{L_d} i_d + \omega \frac{L_q}{L_d} i_q \quad 67$$

$$\frac{di_q}{dt} = \frac{1}{L_q} V_q - \frac{R}{L_q} i_q - \omega \frac{L_d}{L_q} i_d - \frac{\omega\lambda_{pm}}{L_q} \quad 68$$

Article DOI: 10.52589/AJSTE-J8Z7SLJ8
DOI URL: https://doi.org/10.52589/AJSTE-J8Z7SLJ8

The error in i_d current, e_d, per sample time is the same as the time rate of change of i_d current (ie. $\frac{di_d}{dt}$).

$$\frac{di_d}{dt} = e_d = i_d^* - i_d \qquad 69$$

Similarly, the error in i_q current, e_q, per sample time is the same as the time rate of change of i_q current (ie. $\frac{di_q}{dt}$).

$$\frac{di_q}{dt} = e_q = i_q^* - i_q \qquad 70$$

Substituting e_d and e_q in equations 67 and 68, respectively, result to equation 71 and 72 ed.

$$= \frac{1}{L_d}V_d - \frac{R}{L_d}i_d + \omega\frac{L_q}{L_d}i_q \qquad 71$$

$$e_q = \frac{1}{L_q}V_q - \frac{R}{L_q}i_q - \omega\frac{L_d}{L_q}i_d - \frac{\omega\lambda_{pm}}{L_q} \qquad 72$$

Making V_d and V_q subjects of equations 71 and 72 gives

$$V_d = e_d L_d + Ri_d - \omega L_q i_q \qquad 73$$

$$V_q = e_q L_q + Ri_q + \omega L_d i_d + \omega\lambda_{pm} \qquad 74$$

We recall that $K_{ip} = \frac{K_i}{K_p} = \frac{R}{L} \Rightarrow K_i \propto$ R and $K_p \propto L$

Now $e_d = \frac{di_d}{dt} \Rightarrow i_d = \int e_d dt$ 75

Similarly, $e_q = \frac{di_q}{dt} \Rightarrow i_q = \int e_q dt$ 76

Hence $e_d L_d \propto K_p e_d$ and $Ri_d \propto K_i \int e_d dt$ 77

Also, $e_q L_q \propto K_p e_q$ and $Ri_q \propto K_i \int e_q dt$ 78

By making appropriate substitutions of equations 75 to 78 into equations 73 and 74 above, we obtain:

$$V_d = K_p e_d + K_i \int e_d dt - \omega L_q i_q \qquad 79$$

$$V_q = K_p e_q + K_i \int e_d dt + \omega L_d i_d + \omega\lambda_{pm} \qquad 80$$

Equations 79 and 80 give the relation between the d_q- voltages and current errors. Therefore, 79 and 80 represented the mathematical representation of the PI controller that can produce the required d_q- voltages from the current errors.

Article DOI: 10.52589/AJSTE-J8Z7SLJ8
DOI URL: https://doi.org/10.52589/AJSTE-J8Z7SLJ8

Deadbeat Control

In deadbeat control, the two PI controllers in the FOC model were replaced by the deadbeat controller **[12,4]**. The mathematical model of the deadbeat controller was obtained from equations 49 and 50 by setting the reference currents to be the predictive value to be attained in the next sample time, i.e., $i_d = i_d(k+1)$ *and* $i_q = i_q(k+1)$. This makes sense since we wanted the controller to track the reference.

$$i_d(k+1) = \frac{T_s}{L_d}V_d(k) + \left(1 - \frac{RT_s}{L_d}\right)i_d(k) + \frac{\omega(k)L_qT_s}{L_d}i_q(k) \quad 81$$

$$i_q(k+1) = \frac{T_s}{L_q}V_q(k) + \left(1 - \frac{RT_s}{L_q}\right)i_q(k) - \frac{\omega(k)L_dT_s}{L_q}i_d(k) - \frac{\omega(k)\lambda_{pm}T_s}{L_q} \quad 82$$

Making substitutions into equations 81 and 82, we obtain:

$$i_d^* = \frac{T_s}{L_d}V_d(k) + \left(1 - \frac{RT_s}{L_d}\right)i_d(k) + \frac{\omega(k)L_qT_s}{L_d}i_q(k) \quad 83$$

$$i_q^* = \frac{T_s}{L_q}V_q(k) + \left(1 - \frac{RT_s}{L_q}\right)i_q(k) - \frac{\omega(k)L_dT_s}{L_q}i_d(k) - \frac{\omega(k)\lambda_{pm}T_s}{L_q} \quad 84$$

Making V_d the subject of equation 83 and V_q the subject of equation 84, we arrive at equations 85 and 86, respectively

$$V_d(k) = \frac{L_d}{T_s}\left(i_d^*(k) - i_d(k)\right) + Ri_d(k) - \omega(k)L_qi_q(k) \quad 85$$

$$V_q(k) = \frac{L_q}{T_s}\left(i_q^*(k) - i_q(k)\right) + Ri_q(k) - \omega(k)[L_di_d(k) - \lambda_{pm}] \quad 86$$

The block diagram of the deadbeat controller is shown in Figure 8

Figure 8: Block diagram of the proposed deadbeat control model

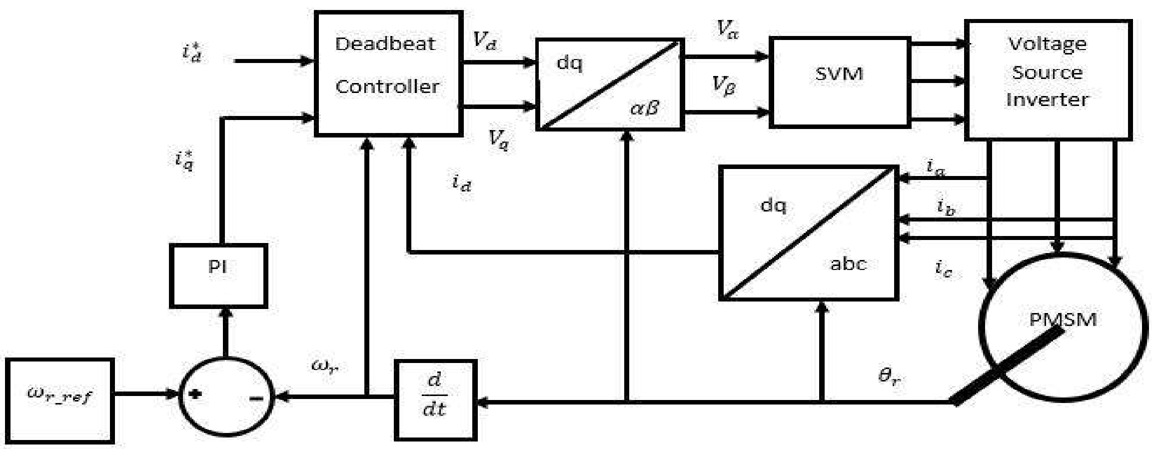

Article DOI: 10.52589/AJSTE-J8Z7SLJ8
DOI URL: https://doi.org/10.52589/AJSTE-J8Z7SLJ8

Advanced Journal of Science, Technology and Engineering
ISSN: 2997-5972
Volume 6, Issue 1, 2026 (pp. 60-87)
www.abjournals.org

Space Vector Modulation

Space Vector Pulse Width Modulation (SVPWM) technique has become very popular due to its higher DC bus voltage utilization and its easy digital realization **[13]**. The idea of SVPWM is based on the representation of the inverter output as space vectors or space phasors. The space vector was defined as:

$$f_s = \frac{2}{3}(f_a + f_b e^{j\frac{2\pi}{3}} + f_c e^{j\frac{4\pi}{3}}) \quad 89$$

Where f_a, f_b, f_c are three-phase quantities that may represent voltage, current, or fluxes. In the case of voltage source inverter modulation, voltage space vectors were considered. Since each inverter switch has only two states (0 or 1) and three-phase inverters have three legs, the total possible switching state combinations were $2^3 = 8$ (000 001 010 011 100 101 110 111). Where "0" means the upper switch was OFF and "1" means the upper switch was ON. Out of the above 8 voltage vectors, the vectors 000 and 111 produce an output voltage of zero in the inverter and hence are known as zero vectors **[8]**. Thus, there were six non-zero or active voltage vectors that were separated 60 degrees apart as shown in Figure 10. Implementation of the SVPWM was done by first calculating the reference voltage and determining the sector in which it lies.

Then the nearest two neighbouring active vectors and a zero vector were utilized to reproduce the reference vector.

Figure 9: Voltage space vector representation

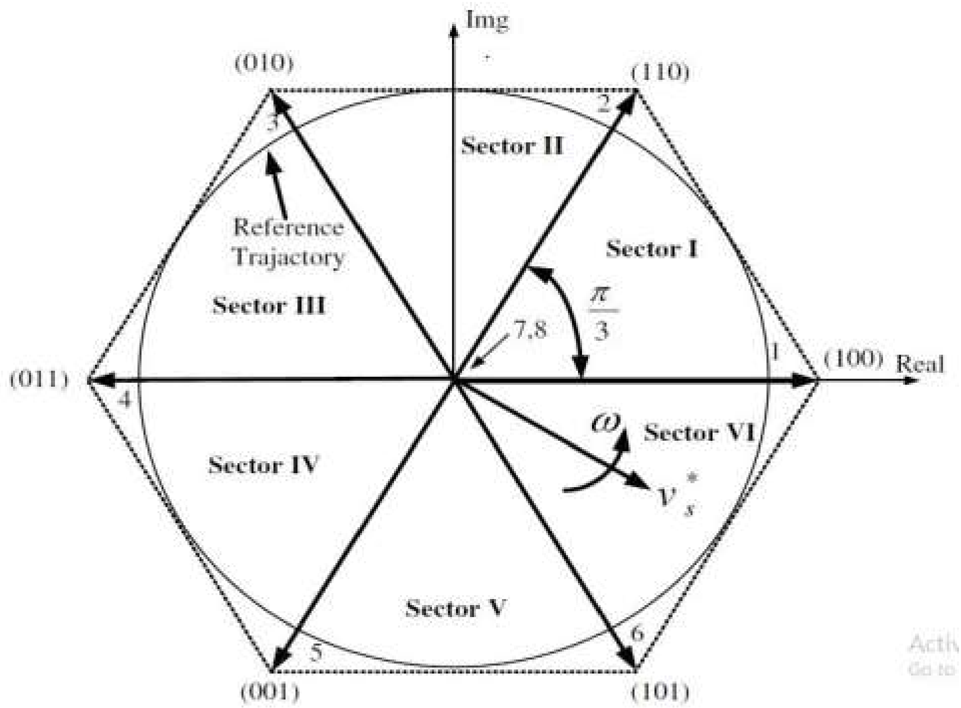

The inverter phase voltage vector and the 8 states were summarized in Table 1below.

Article DOI: 10.52589/AJSTE-J8Z7SLJ8
DOI URL: https://doi.org/10.52589/AJSTE-J8Z7SLJ8

Advanced Journal of Science, Technology and Engineering
ISSN: 2997-5972
Volume 6, Issue 1, 2026 (pp. 60-87)

Table 1: Inverter phase voltage vectors

Switch states	Vector number	Phase voltage space vectors	Voltage symbol
000	7	0	V_7
001	5	$\frac{2}{3}V_{dc}e^{j\frac{4\pi}{3}}$	V_5
010	3	$\frac{2}{3}V_{dc}e^{j\frac{2\pi}{3}}$	V_3
011	4	$\frac{2}{3}V_{dc}e^{j\pi}$	V_4
100	1	$\frac{2}{3}V_{dc}e^{j0}$	V_1
101	6	$\frac{2}{3}V_{dc}e^{j\frac{5\pi}{3}}$	V_6
110	2	$\frac{2}{3}V_{dc}e^{j\frac{\pi}{3}}$	V_2
111	8	0	V_8

After identifying the sector in which the reference voltage falls, the next stage is to calculate the duration of application of each of the active vectors, as well as the zero vector. This was achieved using the equal volt-second principle. The principle of equal volt-second states that the product of the voltage reference and switching is equal to the sum of products of the voltage vectors applied and their period of application, provided the reference was maintained constant in the interval of switching. Suppose the voltage reference was in sector 1, then it can be obtained using V_1, V_2, and V_0. Let the time for each vector be t_a, tb, and t_0, respectively. According to the principle of equal volt-second for sector 1,

$$v_s^* T_s = V_1 t_a + V_2 t_b + V_0 t_0 \tag{90}$$

But $T_s = t_a + t_b + t_0$

The space vectors are given as:

$$v_s^* = |v_s^*|e^{j\alpha}, V_1 = \frac{2}{3}V_{dc}e^{j0}, V_2 = \frac{2}{3}V_{dc}e^{j\frac{\pi}{3}} \text{ and } V_0 = 0 \tag{91}$$

Substituting equation 91 into 90a, we get

$$|v_s^*|e^{j\alpha}T_s = \frac{2}{3}V_{dc}e^{j0}t_a + \frac{2}{3}V_{dc}e^{j\frac{\pi}{3}}t_b \tag{92}$$

Resolving the vectors of equation 92, equating real components, and then imaginary components gives equations 93 and 94.

$$|v_s^*|\cos(\alpha)T_s = \frac{2}{3}V_{dc}t_a + \frac{2}{3}V_{dc}\cos\left(\frac{\pi}{3}\right)t_b \tag{93}$$

Article DOI: 10.52589/AJSTE-J8Z7SLJ8
DOI URL: https://doi.org/10.52589/AJSTE-J8Z7SLJ8

$$|v_s^*|\sin(\alpha)T_s = \frac{2}{3}V_{dc}\sin\left(\frac{\pi}{3}\right)t_b \qquad 94$$

Solving for t_b in 94 and then for t_a in 93, we obtain:

$$t_a = \frac{\sqrt{3}|v_s^*|}{V_{dc}}\sin\left(\frac{\pi}{3}-\alpha\right)T_s \qquad 95$$

$$t_b = \frac{\sqrt{3}|v_s^*|}{V_{dc}}\sin(\alpha)\,T_s \qquad 96$$

$$t_0 = T_s - t_a - t_b \qquad 97$$

The above equations can be generalized for the six sectors as in equations 98 to 100 for k = 1,2,6.

$$t_a = \frac{\sqrt{3}|v_s^*|}{V_{dc}}\sin\left(k\frac{\pi}{3}-\alpha\right)T_s \qquad 98$$

$$t_b = \frac{\sqrt{3}|v_s^*|}{V_{dc}}\sin\left(\alpha-(k-1)\frac{\pi}{3}\right)T_s \qquad 99$$

$$t_0 = T_s - t_a - t_b \qquad 100$$

Having determined the dwell-time (time for which each vector was applied), the next step in the implementation of SVPWM was to determine the switching sequence. In order to reduce switching losses, obtain a fixed switching frequency that was fixed, and optimal harmonic performance, each leg of the inverter should vary its state only once during each period of switching **[4,7]**. To achieve this, the period of switching, T_s, was split into 8 parts. The vector (000) was applied for a quarter of the total time of zero vector ($t_0/4$), then the active vectors follow and are applied for half of their individual time, after which the vector (111) was applied for a quarter of the total time of zero vector ($t_0/4$) in half the total period of switching. The remaining half of the period of switching was a mirror image of the first one. The switching sequence for sector 1 was illustrated in Figure 11 below.

Figure 10: Switching sequence for sector 1.

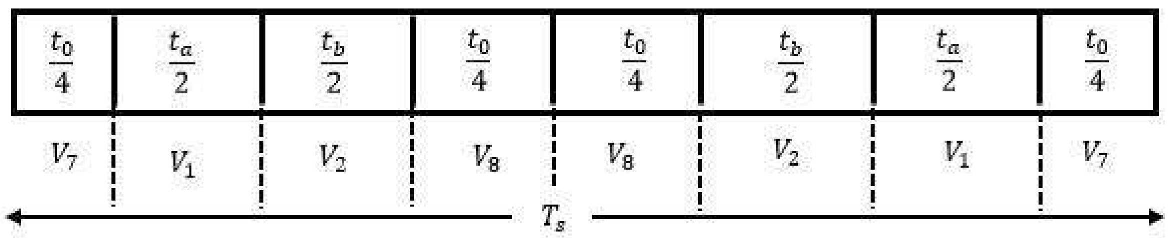

Switching sequences for other sectors are obtained similarly. This method of switching was known as symmetrical SVPWM. **Rectifier and Voltage Source Inverter**

In industries where AC drives are usually applied, the power supply is in three-phase alternating current (AC), while the input to the inverter section of the drive must be direct

Article DOI: 10.52589/AJSTE-J8Z7SLJ8
DOI URL: https://doi.org/10.52589/AJSTE-J8Z7SLJ8

Advanced Journal of Science, Technology and Engineering
ISSN: 2997-5972
Volume 6, Issue 1, 2026 (pp. 60-87)
www.abjournals.org

current (DC). For this reason, there was a three-phase uncontrolled rectifier feeding a three-phase voltage source inverter. However, if power is available in single-phase, it can also be rectified with a single-phase full-bridge uncontrolled rectifier to feed the inverter stage. We considered a three-phase supply in this work. The circuit diagram of the three-phase uncontrolled rectifier is shown in Figure 12.

Figure 11: Circuit three-phase uncontrolled rectifier

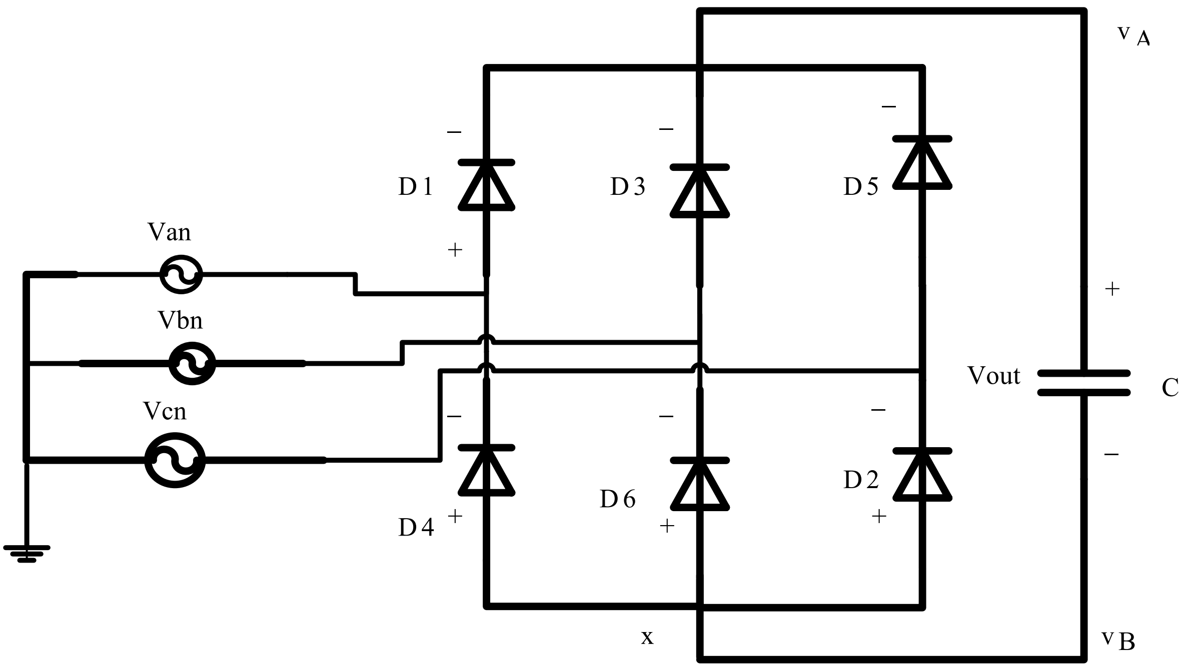

The operation of the rectifier was explained as follows: when $\theta \leq 60°$, V_{an} was higher than both V_{bn} and V_{cn}. Diodes D1 and D2 was forward biased (conducting) while D3, D4, D5, and D6 reverses biased (blocked). Current flows from $V_{an} \rightarrow D1 \rightarrow R \rightarrow D2 \rightarrow V_{cn}$ back to the source. Similarly, when $60° < \omega t \leq 120°$, V_{bn} was higher than both V_{an} and V_{cn}. Diodes D2 and D3 were forward biased (conducting) while D1, D4, D5, and D6 were reverse biased (blocked). Current flows from

$V_{bn} \rightarrow D3 \rightarrow R \rightarrow D2 \rightarrow V_{cn}$ back to the source. The direction of current through the load remains the same during each conduction interval. Table 2 summarizes the operation of the three-phase uncontrolled rectifier circuit.

Table 2: Switching sequence of a three-phase uncontrolled rectifier

S/N	Sector angle, θ	D1	D2	D3	D4	D5	D6
1	$0° < \omega t \leq 60°$	1	1	0	0	0	0
2	$60° < \omega t \leq 120°$	0	1	1	0	0	0
3	$120° < \omega t \leq 180°$	0	0	1	1	0	0

Article DOI: 10.52589/AJSTE-J8Z7SLJ8
DOI URL: https://doi.org/10.52589/AJSTE-J8Z7SLJ8

4	$180° < \omega t \leq 240°$	0	0	0	1	1	0
5	$240° < \omega t \leq 300°$	0	0	0	0	1	1
6	$300° < \omega t \leq 360°$	1	0	0	0	0	1

The average output voltage was given by

$$V_{dc} = V_{out} = \frac{2}{\pi/3}\int_0^{\frac{\pi}{6}} \sqrt{3}V_m cos\omega t \, d(\omega t) = \frac{3\sqrt{3}}{\pi}V_m \quad 101$$

Where V_m represents the peak of the source voltage. The circuit model of a 3-phase voltage source inverter is shown in Figure 13.

Figure 12: Three-phase Voltage Source Inverters

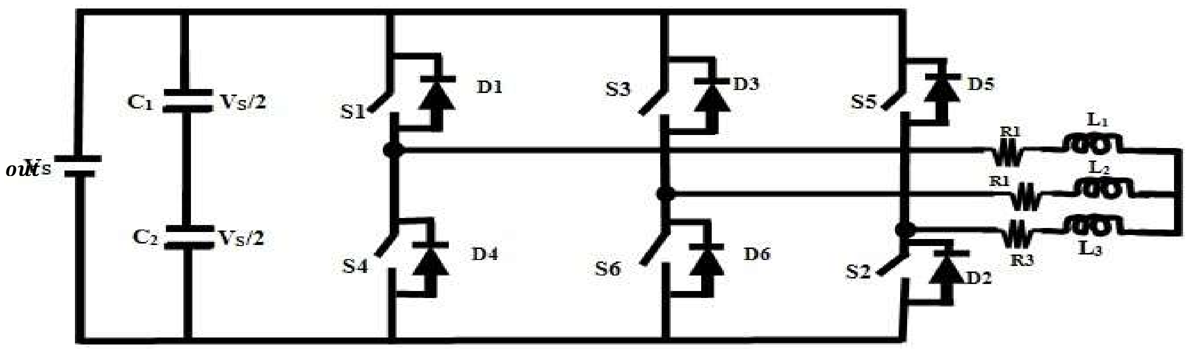

Switching signals generated by the SVPWM discussed in Section 9 were applied to the switching devices in the inverter. For instance, when V_1 (100) was applied, it means that switches S1, S2, and S6 were ON for the time while S3, S4, and S5 were OFF during the same time interval. Similarly, when V_2 (110) was applied for $\frac{t_b}{2}$, S1, S3, S2 were conducting while S4, S5, S6 was OFF. When the zero vector (000) was applied, all the upper switches (S1, S3, S5) were OFF, while applying the zero vector (111) made all the upper switches ON. Summarily, when an upper switch is ON, a lower switch in the same leg must be OFF.

SIMULATION AND RESULTS

The developed algorithms for FOC and DBC were modelled and simulated in MATLAB/Simulink environment (version 2014a). The performance of the models was then tested for step speed with speed reversal. The load torque was maintained at the rated value (20Nm) during the simulations **[5]**. It was evident from the results obtained that the three models have good performance in terms of speed, accuracy, reference tracking, and reduction in ripples. However, a more careful look at the results shows that some of the algorithms perform better than others in some aspects. This section presents the performance of DBC to the standard FOC **[16]**.

Article DOI: 10.52589/AJSTE-J8Z7SLJ8
DOI URL: https://doi.org/10.52589/AJSTE-J8Z7SLJ8

Advanced Journal of Science, Technology and Engineering
ISSN: 2997-5972
Volume 6, Issue 1, 2026 (pp. 60-87)
www.abjournals.org

Simulation Results for FOC

Figure 14 was the d-axis current of the FOC. The current reference was maintained at zero always to ensure that the flux remains constant. The actual current tries to track the reference at all times. The deviation was more magnified than it actually was; for example, the highest deviation was about 5×10^{-17}A, which was almost zero **[14]**.

For a PMSM without saliency in the rotor magnet, the inductance in the q-axis was equal to the inductance in the d-axis, making torque directly proportional to q-axis current. This was why the q-axis current always has the same shape as the torque, but with a lower magnitude. Figure 15 shows that the actual q-axis current follows the reference effectively with little transient during speed reversal.

Figure 13: d-axis current for FOC

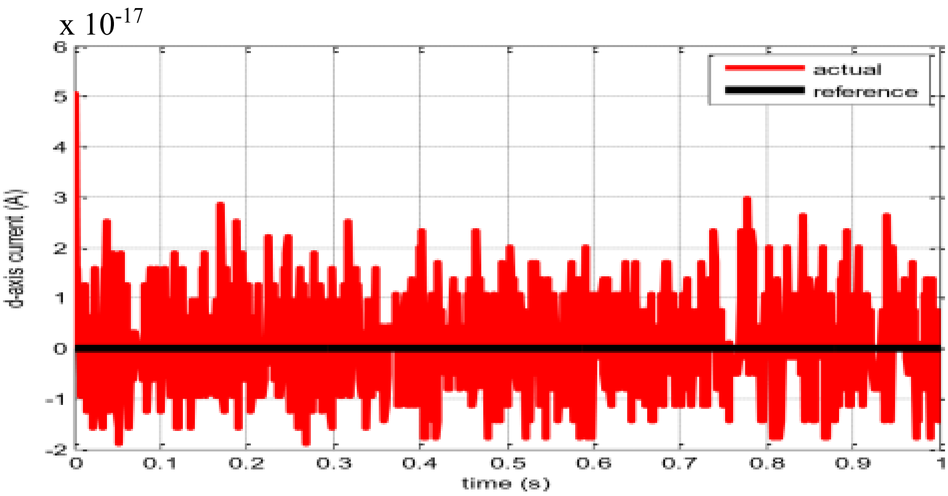

Figure 14: q-axis current for FOC

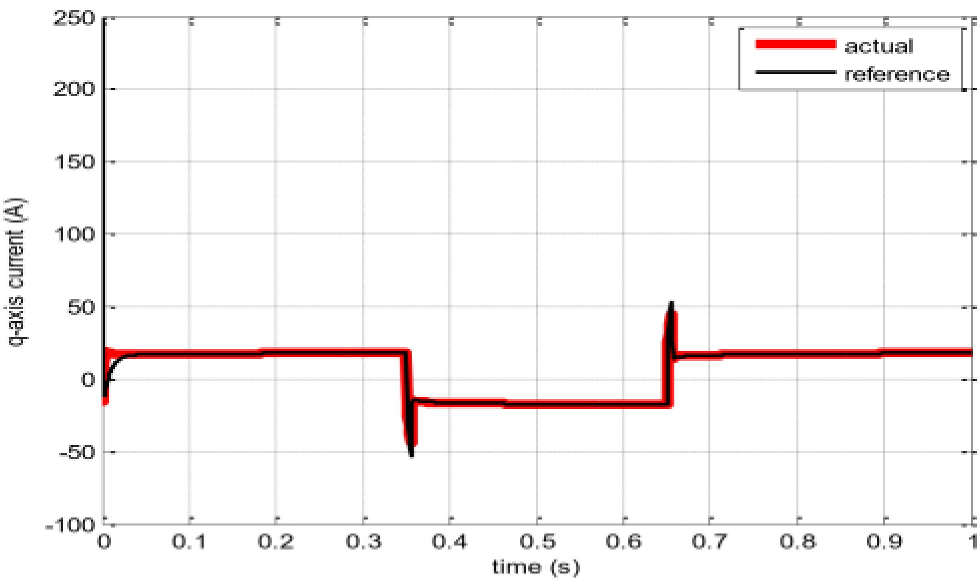

Article DOI: 10.52589/AJSTE-J8Z7SLJ8
DOI URL: https://doi.org/10.52589/AJSTE-J8Z7SLJ8

Figure 15: Motor speed in RPM under FOC

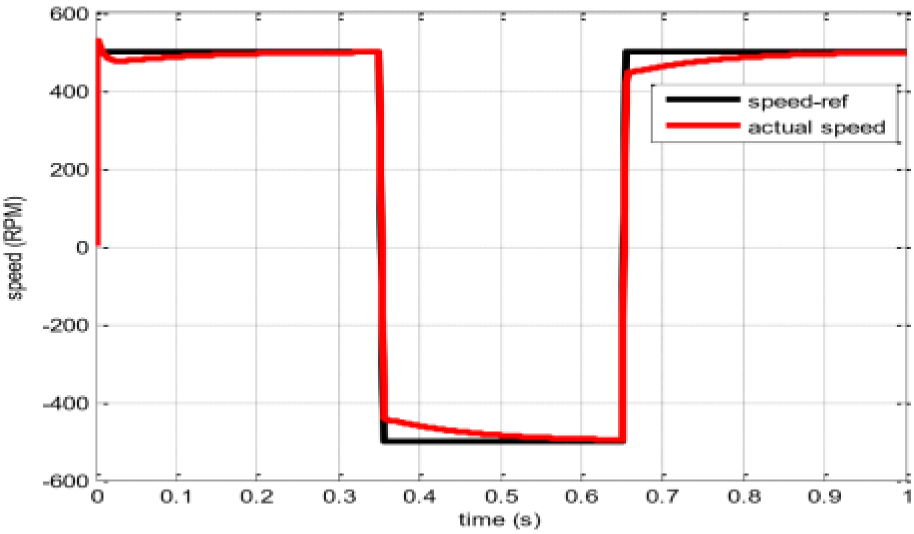

Figure 16 was the speed response of the FOC algorithm. The speed command of magnitude 500RPM was applied at t = 0 seconds and maintained until t = 0.35 seconds. At 0.35 seconds, the command speed suddenly changes to -500RPM, causing speed reversal. The -500RPM command was maintained until 0.65 seconds, when it suddenly went back to 500RPM. The actual speed was able to track the command at t = 0.2 seconds with a very small overshoot at t = 0. The settling time of 0.2 seconds shows that the system has a fast speed response **[3,1]**.

The motor phase currents, as seen in Figure 17, were purely sinusoidal and are displaced from each other by 120 degrees. A current spike was seen and the points of speed reversal, but dies down almost instantly, thereby posing no much threat to the motor coils. During speed reversal, the amplitude of the current remained the same (about 18A) while its direction changed, as can be seen in Figure 17.

Figure 16: Phase currents of the motor under FOC

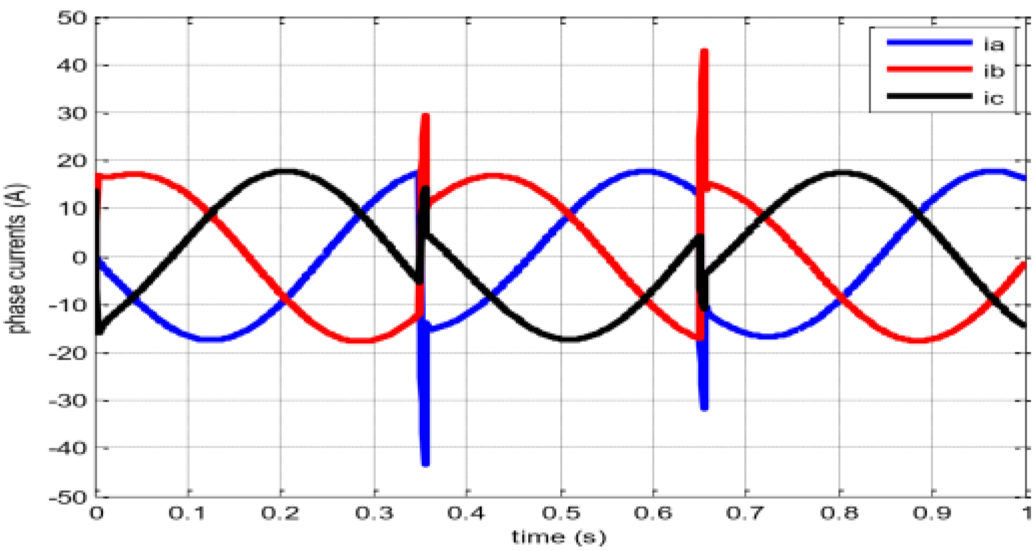

Article DOI: 10.52589/AJSTE-J8Z7SLJ8
DOI URL: https://doi.org/10.52589/AJSTE-J8Z7SLJ8

Simulation Results for DBC

Figure 17: d-axis current for Deadbeat

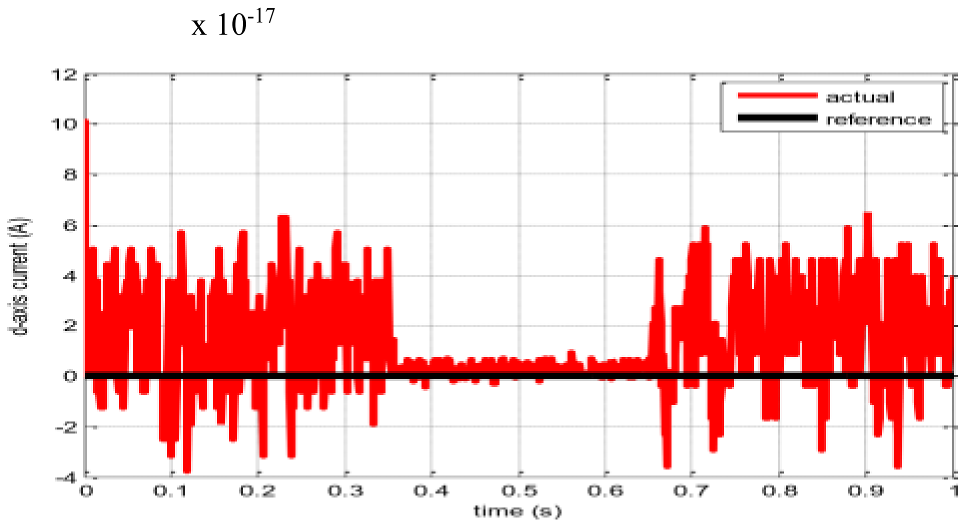

Figure 19 presents the d-axis current for the DBC algorithm. Just like in the FOC, the reference was kept at zero to maintain constant flux. The deviation of the actual current from the reference is very small (of the order 10^{-17}), although it looks more magnified. At the point of speed reversal, the deviation reduced significantly. This reduction also reflects in the phase currents because the phase currents are a combination of d-axis and q-axis currents.

Figure 18: q-axis current for Deadbeat

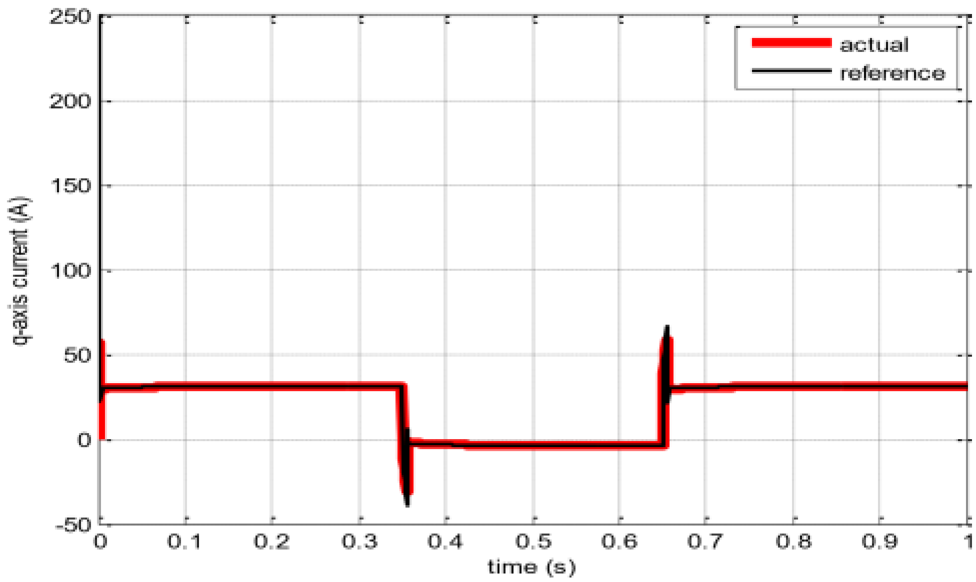

Article DOI: 10.52589/AJSTE-J8Z7SLJ8
DOI URL: https://doi.org/10.52589/AJSTE-J8Z7SLJ8

Advanced Journal of Science, Technology and Engineering
ISSN: 2997-5972
Volume 6, Issue 1, 2026 (pp. 60-87)

Figure 19: Speed of the motor for Deadbeat

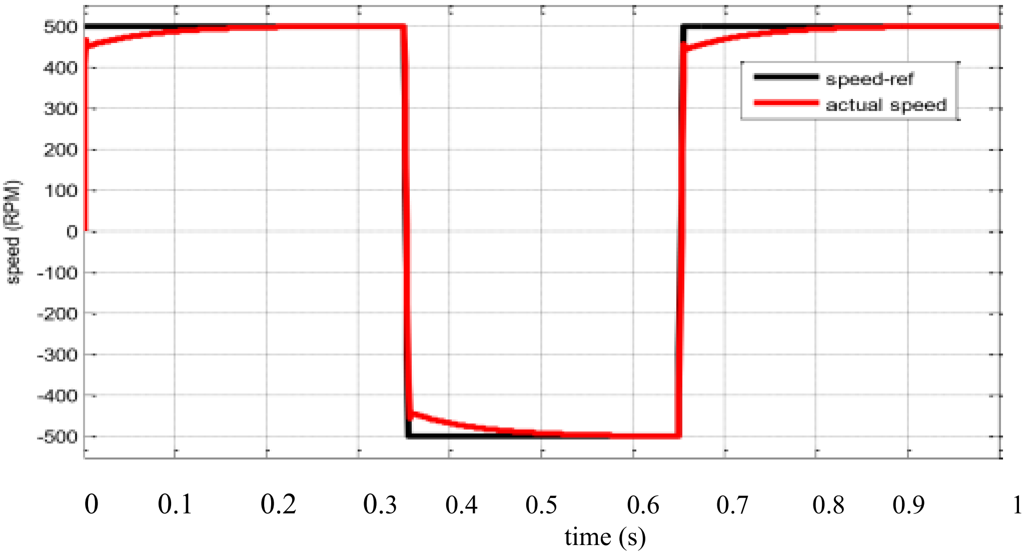

Figure 20: Phase currents (A) for Deadbeat

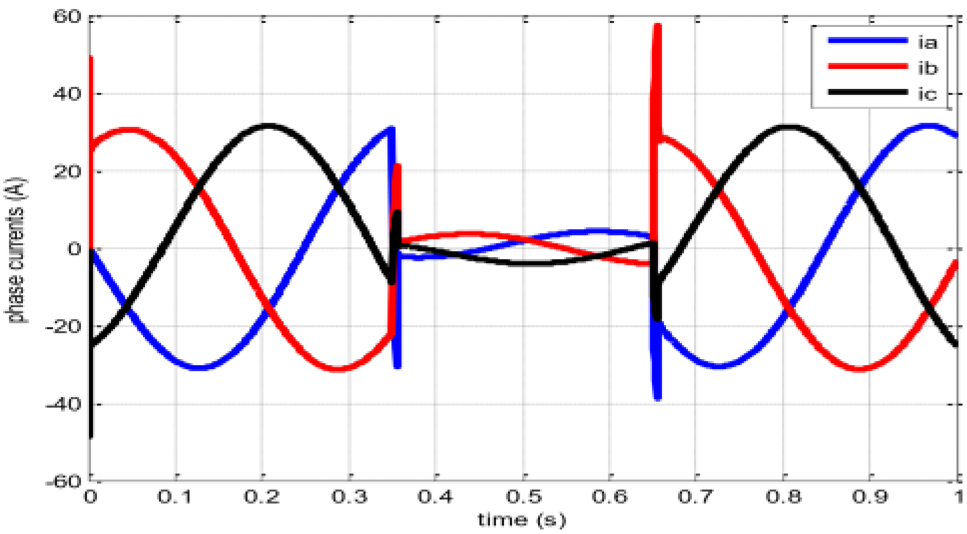

It was seen in Figure 20 that a better tracking of the reference current in the q-axis by the actual current in the q-axis was achieved than that of FOC. Figure 21 was the speed response of the DBC algorithm. The same speed command used in the FOC was also used in the DBC for ease of comparison. The response of the system to the speed command was faster with a settling time of 0.12 seconds. Compared with FOC, which settled at 0.2 seconds, there was 40% increase in the speed of response. In other words, the DBC algorithm was 40% faster than the FOC. The phase currents of Figure 22 were also purely sinusoidal and displaced 120 degrees from one another. There was a drop in phase current magnitude during speed reversal, which was due to the drop in current of the d-axis.

Article DOI: 10.52589/AJSTE-J8Z7SLJ8
DOI URL: https://doi.org/10.52589/AJSTE-J8Z7SLJ8

DISCUSSIONS

The implementation of Space Vector Pulse Width Modulation (SVPWM) was vital for optimizing inverter control in PMSMs, enabling reduced switching losses, harmonic suppression, and better dynamic performance. The inverter's switching period was divided into eight (8) segments, applying zero and active vectors in a sequence that minimizes device stress and electromagnetic interference. In rectifier operation, switching states depend on the rotor angle, ensuring continuous current conduction and minimal torque ripple. SVPWM modulates inverter switches to produce desired voltage vectors, with transitions adhering to an optimal sequence for efficiency **[15]**.

Within the Field-Oriented Control (FOC) framework, the d-axis current was maintained at zero with high accuracy, and the torque, proportional to the q-axis current, remains stable during speed reversals. The system demonstrates rapid speed response, reaching 500 RPM within 0.2 seconds, with sinusoidal phase currents and quick transient dissipation. Comparatively, the Direct Back-EMF Control (DBC) algorithm exhibits a faster response, settling in approximately 0.12 seconds, 40% quicker than FOC, and also maintains sinusoidal currents with minor drops during reversals **[17]**.

Recent advances enhance PMSM drive efficiency and responsiveness by proactively optimizing switching actions based on system models. Integrating these techniques with SVPWM can significantly improve performance in high-demand applications.

CONCLUSIONS

In this study, the dwell-time for each voltage vector was initially determined, enabling the next step of implementing Space Vector Pulse Width Modulation (SVPWM) by establishing an optimal switching sequence. To minimize switching losses, maintain a fixed switching frequency, and enhance harmonic performance, each inverter leg was designed to change state only once per switching period. This was achieved by dividing the switching period $T_s$into eight segments, with the zero vector (000) applied for one-quarter of $t_0 the\ switching\ period$, followed by active vectors occupying half of their respective durations, and then the zero vector (111) applied for the remaining quarter in half the switching period. The second half of the period mirrored the first, ensuring symmetrical operation.

The operation of the rectifier was analyzed across different angle regions: for $\theta \leq 60°$, $V_{an}$was higher than $V_{bn}$and V_{cn}, causing diodes D1 and D2 to conduct, with current flowing from V_{an}through D1, the load resistor, D2, and back to V_{cn}. Similarly, for $60° < \theta \leq 120°$, $V_{bn}$was dominant, leading to conduction through D3 and D2, with current flow adjusted accordingly. During each conduction interval, the current direction through the load remained consistent. The switching signals generated by the SVPWM modulated the inverter switches such that specific switch combinations applied the desired voltage vectors, for example, applying $V_1(100)$involved turning on switches S1, S2, and S6, while involving 2 switches S1, S2, and S3. Zero vectors (000 and 111) corresponded to all upper switches off or on, respectively, with the rule that when upper switches were on, the corresponding lower switches in the same leg were off.

Article DOI: 10.52589/AJSTE-J8Z7SLJ8
DOI URL: https://doi.org/10.52589/AJSTE-J8Z7SLJ8

The d-axis current within the Field-Oriented Control (FOC) was maintained at zero to stabilize flux, with the actual current closely tracking the reference. Deviations were negligible, around 5×10^{-17}A. For a non-salient rotor PMSM, the equality of inductances in the d- and q-axes meant the torque was directly proportional to the q-axis current, which followed the reference with minimal transient disturbance during speed reversals. The system's speed response demonstrated rapid tracking: a 500 RPM command was achieved within 0.2 seconds, with the actual speed accurately following the command even during reversals, exhibiting only minor overshoot.

The phase currents remained sinusoidal, separated by 120°, with brief current spikes at speed reversal points that rapidly subsided, posing no significant risk to the motor. During these reversals, the current amplitude stayed approximately 18 A, with the current direction shifting accordingly.

The D-axis Based Control (DBC) algorithm also maintained the d-axis current at zero with deviations on the order of 10^{-17}, and showed a significant reduction in deviation during speed reversal. Compared to FOC, the DBC achieved a faster system response, with a settling time of approximately 0.12 seconds, about 40% quicker than the 0.2 seconds observed with FOC. The phase currents under DBC remained sinusoidal and balanced, though a slight current drop occurred during speed reversal, attributed to the decrease in d-axis current.

Overall, the proposed predictive current control strategies demonstrated superior dynamic performance, rapid response, and effective current tracking, validating their potential for advanced control of PMSMs in high-performance applications.

Further research could explore the implementation of a Model Predictive Current Control (MPC) algorithm, which forecasts the upcoming dq-currents to directly determine the next stator voltage reference for the machine. Additionally, a comparison among the three control strategies, FOC, DBC, and MPC, can be conducted.

REFERENCES

1. Al-Ali, A. K., et al. (2021). Robust Control of PMSM Drives Based on Adaptive FOC Techniques. IEEE Transactions on Power Electronics, 36(5), 5679-5690. https://doi.org/10.1109/TPEL.2020.3039609
2. Chen, L., Zhao, Y., & Liu, Q. (2021). Ripple reduction techniques in PMSM drives using advanced control algorithms. Electric Power Systems Research, 198, 107477. https://doi.org/10.1016/j.epsr.2021.107477
3. Kim, J., Lee, S., & Park, H. (2021). "Comparison of Field-Oriented Control and Direct Back-EMF Control in PMSM Applications." IEEE Transactions on Industrial Electronics, 68(9), 8808-8818. https://doi.org/10.1109/TIE.2021.3064762
4. Kumar, P., & Singh, R. (2023). "Comparative analysis of FOC and predictive control schemes for PMSM drives." IEEE Access, 11, 16578-16588. https://doi.org/10.1109/ACCESS.2023.3267894
5. Kumar, R., & Singh, A. (2020). Comparative Analysis of FOC and DBC for PMSM Drives in MATLAB/Simulink Environment. IEEE Transactions on Industrial Electronics, 67(4), 2912-2922. https://doi.org/10.1109/TIE.2019.2917432

Article DOI: 10.52589/AJSTE-J8Z7SLJ8
DOI URL: https://doi.org/10.52589/AJSTE-J8Z7SLJ8

6. Kumar, S., & Patel, R. (2021). Modeling of inductance profiles in salient pole machines considering rotor position and magnetic saturation. IEEE Transactions on Industrial Electronics, 68(9), 8723-8732. https://doi.org/10.1109/TIE.2021.3102794
7. Lee, J., & Kim, S. (2023). Impact of reference frame transformations on PMSM control and modeling. IEEE Transactions on Industrial Electronics, 70(4), 3405-3414. https://doi.org/10.1109/TIE.2023.3214567
8. Li, M., & Liu, X. (2023). "Development of dead-beat predictive current control for high-performance PMSM drives." IEEE Transactions on Industrial Informatics, 19(2), 1245-1254. https://doi.org/10.1109/TII.2022.3177944
9. Liu, X., Chen, H., & Li, J. (2021). Simulation and Implementation of Direct Torque Control for PMSM Using MATLAB/Simulink. International Journal of Electrical Power & Energy Systems, 126, 106569. https://doi.org/10.1016/j.ijepes.2020.106569
10. Nguyen, T. T., & Chen, M. (2023). "Model-Based Optimization Strategies for PMSM Drive Efficiency." Renewable Energy and Power Systems Journal, 15(2), 105-118. https://doi.org/10.1234/reps.2023.01502
11. Patel, D., & Mehta, V. (2019). Rotating reference frame analysis of PMSMs for efficient control design. International Journal of Electrical Power & Energy Systems, 112, 105272. https://doi.org/10.1016/j.ijepes.2019.105272
12. Singh, S., & Verma, S. (2023). Optimization of PMSM Control Strategies for Improved Dynamic Response. Electronics, 12(8), 1764. https://doi.org/10.3390/electronics12081764
13. Sun, J., Wang, Y., & Zhou, Z. (2020). "Self-tuning field-oriented control of PMSM based on adaptive PI controllers." IEEE Transactions on Industrial Electronics, 67(9), 7464-7474. https://doi.org/10.1109/TIE.2020.2972489
14. Wang, H., & Chen, L. (2020). Coordinate transformations and simplified modeling approaches for PMSMs in digital control. Journal of Electrical Engineering & Technology, 15(2), 1021-1030. https://doi.org/10.1007/s42835-020-00385-1
15. Wang, H., & Chen, Y. (2022). Ripple suppression and optimal tuning strategies in PMSM control systems. IEEE Transactions on Power Systems, 37(6), 4568-4578. https://doi.org/10.1109/TPWRS.2022.3179502
16. Zhang, L., Wang, H., & Liu, Y. (2022). "Advanced SVPWM Techniques for High-Performance PMSM Drives." IEEE Transactions on Power Electronics, 37(4), 4521-4533. https://doi.org/10.1109/TPEL.2022.3145678
17. Zhang, Y., Li, X., & Wang, H. (2022). "Advanced control strategies for permanent magnet synchronous motors: A review." IEEE Transactions on Power Electronics, 37(4), 4152-4164. https://doi.org/10.1109/TPEL.2021.3108927
18. Zhao, Y., & Sun, Y. (2023). Enhanced Back-EMF Estimation Methods for PMSM Speed Control. IEEE Access, 11, 64456-64466. https://doi.org/10.1109/ACCESS.2023.3282457

Article DOI: 10.52589/AJSTE-J8Z7SLJ8
DOI URL: https://doi.org/10.52589/AJSTE-J8Z7SLJ8